CLOUD COVER DETERMINATION IN POLAR REGIONS FROM SATELLITE IMAGERY

R.G. Barry, J.R. Key, and J.A. Maslanik

Cooperative Institute for Research in Environmental Sciences
and
Department of Geography
University of Colorado, Boulder

Semi-Annual Report
to
NASA Climate Program

Grant: NAG-5-898

15 June 1988

1.0 Introduction

The principal objectives of this project are

1) to develop sutable validation data sets to evaluate the effectiveness of the ISCCP operational algorithm for cloud retrieval in polar regions and to validate model simulations of polar cloud cover;
2) to identify limitations of current procedures for varying atmospheric surface conditions, and to explore potential means to remedy them using textural classifiers;

and 3) to compare synoptic cloud data from a control run experiment of the GISS climate model II with typical observed synoptic cloud patterns.

The following sections list the current investigations underway and summarize the progress made to date since the last semi-annual report.

2.0 Comparison of Modeled and Observed Cloud Cover in the Arctic

The Goddard Institute for Space Studies (GISS) general circulation model was used to predict cloud cover in the Arctic. Monthly average cloud fractions calculated by the GISS model were evaluated in terms of temporal and spatial distributions, and were compared to observed cloud amounts. The GISS model cloudiness in the Arctic was found to demonstrate the seasonal variability expected based on observational data, but at a much reduced range in the central Arctic. As with the observational data, the zone of maximum cloud cover moves north in the summer, but the calculated amounts are less than expected by about

10-20%. The GISS results indicate that, while most of the cloud cover would appear to be due to large-scale processes, there is some evidence that reduced ice concentration in summer may give rise to some low-level cloud on a limited regional basis. The attached paper provides additional details.

3.0 Test Data Sets

The data being used to investigate the spectral and textural properties of polar clouds consist of a set of geolocated and first-order calibrated AVHRR data merged with digital passive microwave imagery acquired by the Nimbus-7 Scanning Multichannel Microwave Radiometer. The attached draft paper describes the purpose, creation, and use of these data. Collaborative analysis and publication of results with Professor E. Raschke, University of Koln, is planned.

4.0 Catalog of Spectral and Textural Signatures for Polar Clouds and Surfaces

The design and testing of algorithms for cloud mapping requires an understanding of the spectral and textural properties of the features to be classified. The objective of this task is to improve our understanding of these characteristics for polar clouds, snow, and sea ice by recording the means and standard deviations of these features as derived from multispectral AVHRR data. To achieve this objective, training areas representing a variety of cloud and surface combinations were selected from the merged AVHRR and SMMR passive microwave data sets. The

statistical characteristics of these training areas in terms of spectral reflectance and temperature as well as textural properties were summarized and recorded.

Comparison of this "catalog" of spectral and textural information with other published data show good agreement, although differences increase as the homogeneity of the training area decreases. For example, clouds of a given class that exhibit varying optical depths yield different spectral signatures than is the case for optically thick cloud. The resulting large standard deviation around the class mean is a likely source of error, and increases the difficulty of objectively evaluating the performance of different classification schemes. To help alleviate these problems, a fuzzy-sets classification routine was developed and tested and a means of developing artificial data sets was devised. This work will be described in the next semi-annual progress report.

5.0 Artificial Data Sets

In order to test the sensitivity of cloud classification algorithms, a control data set with known characteristics is needed. We are developing a series of such data sets which range in complexity from very simple geometric representations of clouds and surfaces with no internal spectral variation to very complex cloud/surface models which have free-form shapes with both spectral and textural characteristics. Surface types are snow-covered and snow-free land, open water, and sea ice. Cloud layers are classified as low, middle, and high, where levels are

defined by AVHRR channel 4 brightness temperatures. Data for each region are then generated for each AVHRR and SMMR channel as well as sea ice concentration using empirically-derived statistics and random-number generators based on uniform, Gaussian, and lognormal distributions.

Testing will be done on the effects of varying the proportion and location of the surface/cloud types, the type of distribution assumed for the classes, whether or not these distributions overlap in spectral and textural space, and the class characteristic values. These distribution-related changes are particularly important in the testing of maximum likelihood classifiers.

6.0 Coherence and Threshold Methods

In anticipation of and justification for the spatial and temporal tests of the ISCCP algorithm, the spatial and temporal coherence tests have been implemented in an attempt to determine clear sky radiances for each pixel over the period. Additionally, we are currently investigating the possibility of setting thresholds dynamically, based on information contained within the image itself, for use in the ISCCP algorithm.

6.1 Spatiotemporal Coherence

In the last report, we described the application of the spatial coherence method of Coakley and Bretherton (1982) to polar data. To aid further in the determination of clear sky radiances, locations may be examined for their variation in time.

Scenes which do not vary significantly from the day before and the day after are assumed to be clear, and a clear sky radiance for the time period can be set equal to the mean or extremum of the series. The feet of the arch are identified in the same manner as in the spatial coherence method. Figure 1 shows temporal coherence plots for two three-day periods. Points with low standard deviations generally represent clear pixels. Problems with temporal coherence occur primarily with stationary cloud systems. Such systems may exhibit high temporal coherence over a short time period (i.e. a few days). Lengthening the time series will, of course, alleviate this problem.

Spatial and temporal coherence tests may be combined for the purpose of identifying which feet of the spatial coherence arch represent clear sky conditions. Those locations which have a low spatial standard deviation on any given day AND a low temporal standard deviation for any three-day period which includes that day are labeled "clear". In this manner, a clear sky radiance map can be constructed for the five day period where each value represents a clear sky value on one or more (in this case an average) of five days, or possibly none at all if clouds persist.

This spatiotemporal coherence method was applied to each pixel in a $(250\ km)^2$ region east of Novaya Zemlya. The method labels those pixels which have low standard deviations in both time and space as clear. A visual comparison of these maps verified that those pixels labeled "clear" in a manual interpretation were generally labeled "clear" by the spatiotemporal coherence method. However, stationary cloud

systems which were also uniform in texture were mislabeled as clear. Figure 2 gives an example of this problem.

6.2 Dynamic threshold

To allow for the influence of cloud size on classification, Coakley (1987) developed a dynamic threshold method for the Pacific Ocean where an infrared threshold is adjusted to achieve the highest correlation between the threshold-derived cloud cover and the mean emitted radiance for mesoscale-sized subregions within the scene. Unlike the spatial coherence method, the dynamic threshold method requires no pixel to be completely cloud-covered or cloud-free. Like the spatial coherence method, the dynamic threshold method assumes a linear relationship between emitted radiances and fractional cloud cover, and is therefore inappropriate for systems like convective ensembles or cirrus clouds, where the relationship is generally multivalued and nonlinear.

In order to test whether the dynamic threshold method could be used to provide more realistic thresholds than are currently applied in the ISCCP algorithm, spatial coherence diagrams have been constructed from the AVHRR imagery for consecutive days. Thresholds were then determined using the dynamic threshold method. The actual threshold chosen is the one which produced the maximum correlation between mean radiance and cloud fraction for subregions of size $(50\ km)^2$. Results of this approach demonstrate that improvements can be achieved using the dynamic thresholding process as opposed to more restrictive

parameterizations of thresholds.

While the dynamic threshold method can theoretically be extended to any number of clouds layers and surface types, such an extension would produce a series of simultaneous equations equal to the number of unknowns. A unique solution for each of n unknowns would require n independent spectral channels. Unfortunately only channels 1 or 2, 3, and 4 (or 5) may be considered sufficiently independent so that the number of unknowns is limited to three. An algorithmic solution to this problem is at least theoretically possible, and is being considered as a possible route to improve classification of mixtures of cloud layers and surface types. If a region is divided into small enough subregions such that each contains pixels which belong to only two feet of the spatial coherence arch, then the dynamic threshold method may be applied separately to each group of subregions which contain only one surface and one cloud layer. This method was tested here on regions 48 pixels square or $(240km)^2$ with subregions $(30\ km)^2$ for a total of 36 pixels per subregion and 64 subregions per region, an example of which is given in Figure 3. Evaluation of the results of this test is currently underway.

7.0 Modifications to the ISCCP Algorithm

A thoroughly-tested version of the ISCCP algorithm for low- and mid-latitudes has been applied to polar data by Rossow (1987). The algorithm misses approximately 20% of the cloud (Rossow, 1987, personal communication). Problems cited include:

"real" cloud amount is high which forces the algorithm to use more extreme values for clear sky radiances; no distinction is made between snow-covered and snow-free land, or sea ice and open water in setting thresholds; thresholds were not "tuned" to the low radiances encountered in polar regions; and no adjustments were made for solar zenith angle.

Modifications to the basic ISCCP algorithm are being made to address these problems directly. Threshold values in the spatial and temporal variation tests are being adjusted to take into account the similarity in brightness temperatures between low cloud and sea ice. Adjustments are also necessary to deal with varying surface types within regions and subregions. Surface types are determined with a land mask, SMMR 37 GHz (horizontal) data, and SMMR-derived sea ice concentration.

The basic ISCCP algorithm assumes a constant surface type over the five-day period. In most cases, this assumption is valid. However, snow melt in the spring and snowfall in late summer are particular problems for this algorithm. Movement of sea ice into or out of a region will cuase similar problems. In both cases, emissivities of the surface change, thereby affecting the response in the thermal channels. Additionally, albedos change dramatically so that those portions of the algorithm which incorporate visible data will be affected the most. The problem lies in the determination of the clear sky composite maps for the visible and thermal channels. If, for example, sea ice moved into a region on the last of day of the period, the average albedo making up the clear sky value would be significantly

affected. If the algorithm detected this event and instead chose an extreme (minimum albedo) for the composite value from the first four days, this last day pixel would be labeled "cloud" in the final bispectral threshold test.

In the algorithm specifications (Rossow, 1987) the compositing step is to use five-day means if there are enough clear pixels or, if not, 30-day means and extremum. In the polar regions, surface characteristics may be too variable for the use of 30-day values to be valid, particularly in summer when sea ice motion increases and concentration changes rapidly. In late summer, snow may occur at any time. Therefore, in the modified version of the algorithm, it is assumed that pixels within a reasonably small spatial area on the same day and of the same surface type will be no less similar than the same pixel up to thirty days later.

Additionally, tests are being performed on the utility of incorporating a third channel in the analysis - AVHRR channel 3. In spite of the fact that this channel is sometimes noisy, and that there is a reflected component in the daytime images, this spectral band is particularly useful in distinguishing low cloud from sea ice.

8.0 Summary

In the first six months of this first project year a methodology was developed for combining AVHRR and SMMR data. These data were calibrated and registered to a polar sterographic projection for subsequent digital analysis. Cloud cover and

surface types were manually interpreted, viewing angle effects were examined, and the development of a catalog of spectral and textural properties of polar clouds and surfaces was begun. Additionally, cloud analysis and clustering methods such as Coakley and Bretherton's spatial coherence and the fuzzy sets approach were implemented.

In the second half of the year, work has continued on the catalog of spectral and textural features, where new combinations of the calibrated AVHRR data (i.e. ratios and differences of AVHRR channels) were included in the analysis and data from two seven-day sequences of imagery for two areas of the Arctic were studied. The spatial coherence method was extended to include time ("temporal coherence") and space and time ("spatiotemporal coherence"). These methods are being examined to gain further insight into the spatial and temporal features of polar clouds and surfaces as they effect the functionality of the ISCCP algorithm, which was implemented here and is currently undergoing testing and modification.

The relationship between theoretical and empirical approaches was examined with the GISS general circulation model, where the spatial and temporal distributions of monthly average cloud fraction were compared to observed cloud amounts. The sensitivity of the ISCCP algorithm and clustering procedures is being tested through the use of synthetic data sets where statistical and geographical characteristics of image data are carefully controlled.

9.0 Future Work

During the next year of this two-year project, we will integrate the procedures developed during the first year and apply them to additional data, in particular winter (January) data for the Arctic and both summer and winter data for the Antarctic. Statistical distributions of the spectral and textural features of polar clouds and surfaces will be analyzed, as these have important implications for the use of statistical classifiers such as maximum likelihood method commonly applied in remote sensing.

The results from the statistical analyses of empirical data will help guide the development of synthetic data sets, which in turn will aid in the development of cloud analysis algorithms. Synthetic data sets have many potential uses and can include fuzzy boundaries between classes (possibly incorporating the fractal nature of cloud edges) and texture. These possibilties will be examined.

Work will continue on the ISCCP algorithm testing and modification for use in the polar regions. As described in this report, a number of problems with the application of this algorithm remain unsolved.

References

Coakley, J.A., Jr., 1987. "A dynamic threshold method for obtaining cloud cover from satellite imagery data," J. Geophys. Res., 92, no. D4, 3985-3990.

Coakley, J.A., and F.P. Bretherton, 1982. "Cloud cover from high-resolution scanner data: detecting and allowing for partially filled fields of view," J. Geophys. Res., 87, no. C7, 4917-4932.

Raschke, E., 1987. "Report of the ISCCP workshop on cloud algorithms in the polar regons," National Institute for Polar Research, WCP-131, WMO/TD-No. 170, Tokyo, Japan, 19-21 August 1986.

Rossow, W.B., 1987. "Application of ISCCP cloud algorithm to satellite observations of the polar regions," in Raschke, E., 1987. "Report of the ISCCP workshop on cloud algorithms in the polar regons," National Institute for Polar Research, WCP-131, WMO/TD-No. 170, Tokyo, Japan, 19-21 August 1986.

Rossow, W.B., 1987. "Preliminary documentation for ISCCP C1 data set", Pilot Climate Data System, Goddard Institue for Space Studies, NASA.

Rossow, W.B., F. Mosher, E. Kinsella, A. Arking, M. Desbois, E. Harrison, P. Minnis, E. Ruprecht, G. Seze, C. Simmer, and E. Smith, 1985. "ISCCP cloud algorithm intercomparison," J. Clim. Appl. Meteor., 24, 877-903.

List of Figures

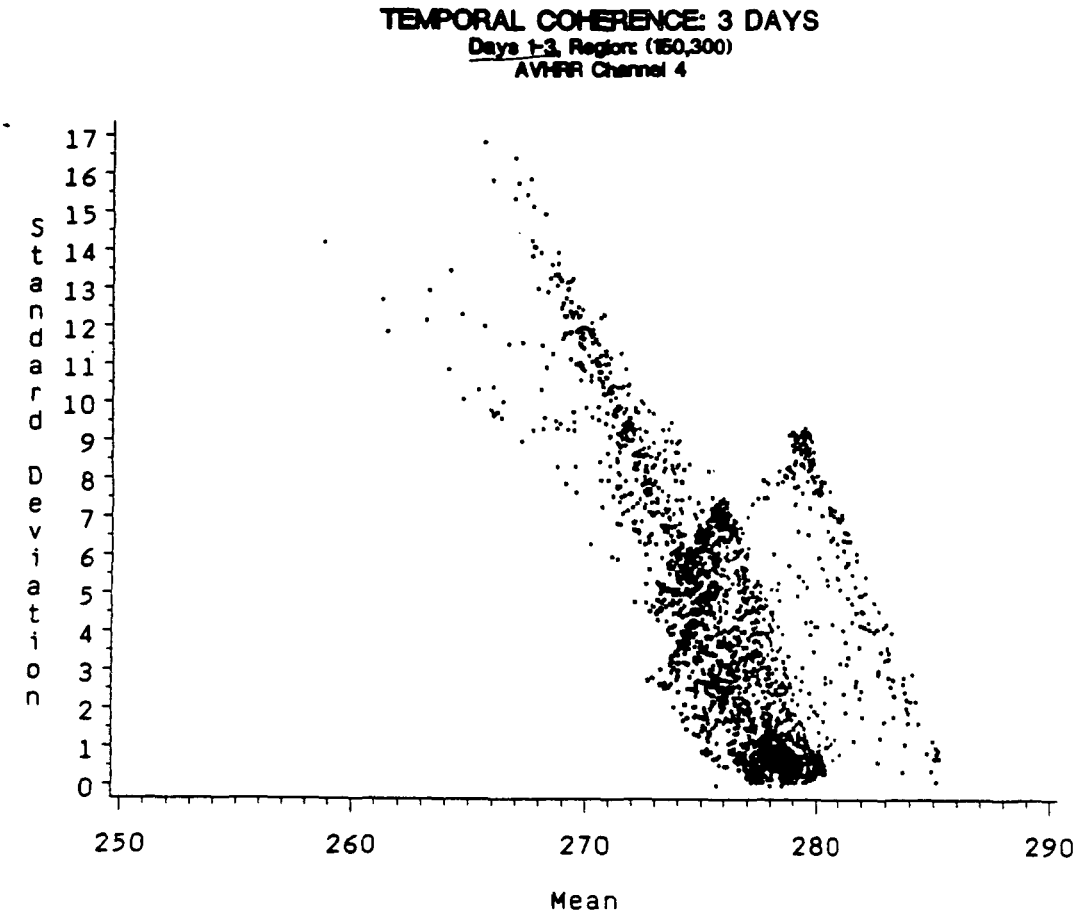
TEMPORAL COHERENCE: 3 DAYS
Days 1-3, Region: (150,300)
AVHRR Channel 4
Standard Deviation
0
1
2
3
4
5
6
7
8
9
10
11
12
13
14
15
16
17
250
260
270
280
290
Mean

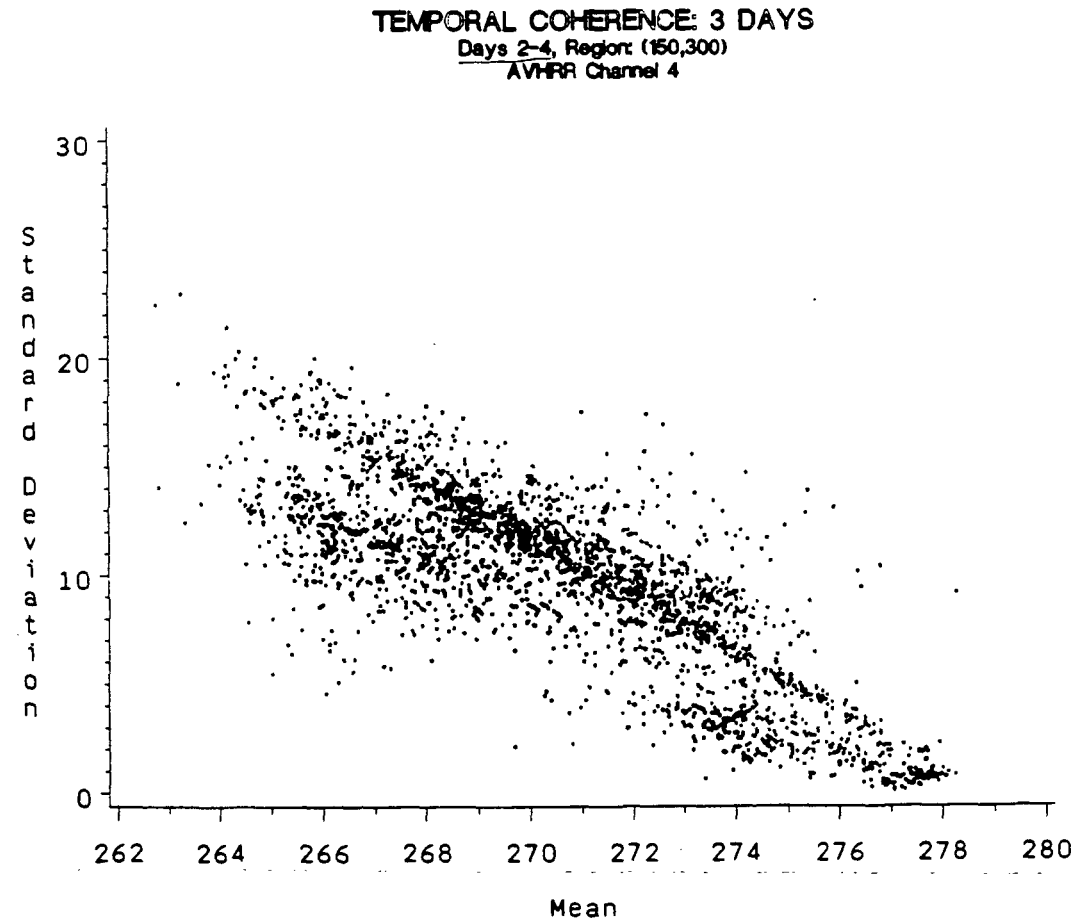
TEMPORAL COHERENCE: 3 DAYS
Days 2-4, Region: (150,300)
AVHRR Channel 4
Standard Deviation
0
10
20
30
262
264
266
268
270
272
274
276
278
280
Mean

Fig. 1.

SPATIOTEMPORAL COHERENCE AND MANUAL INTERPRETATION

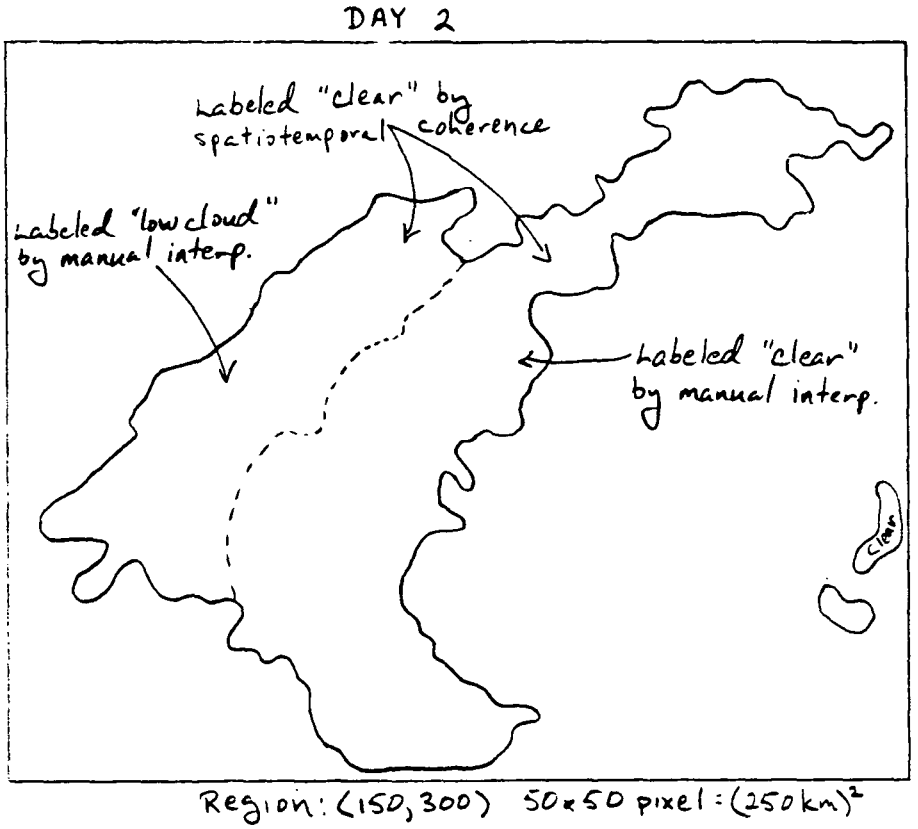

Fig. 2

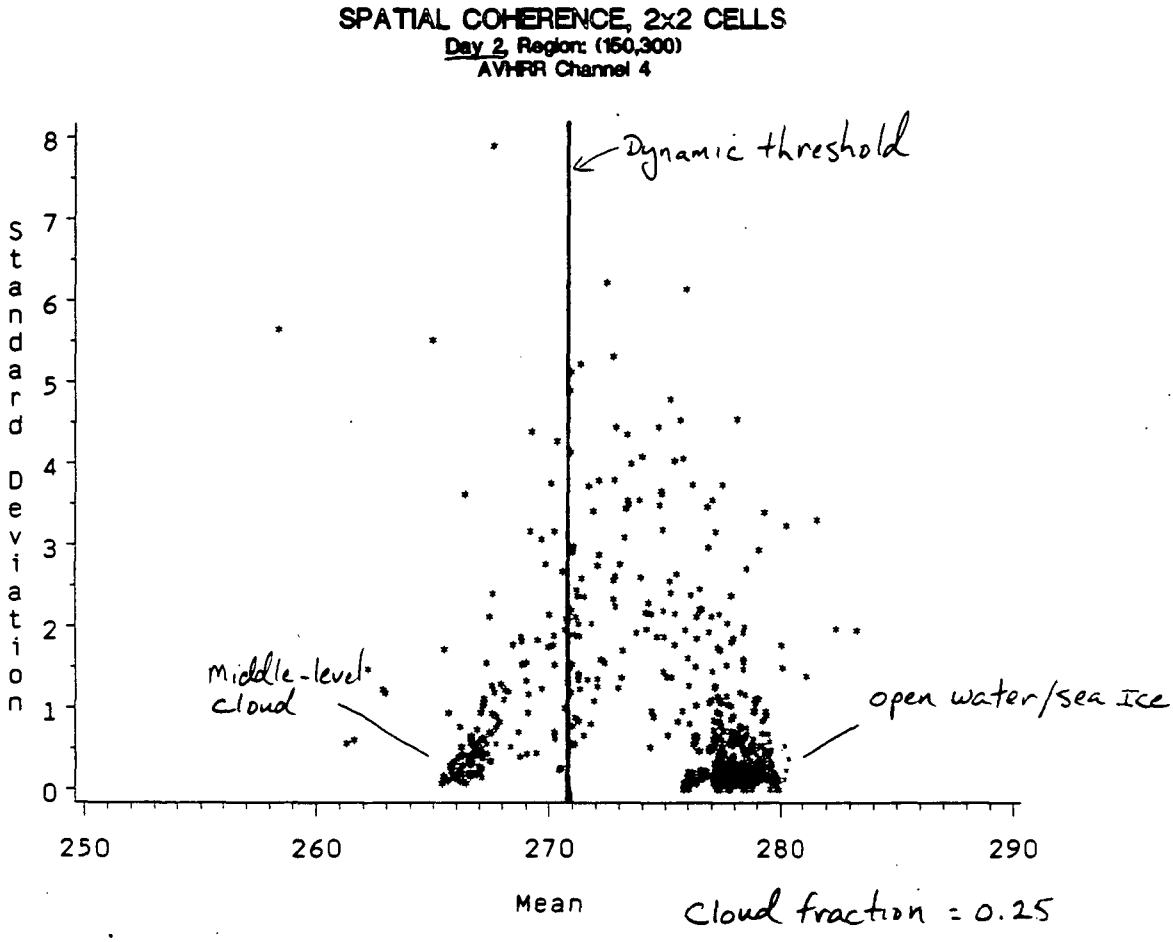
SPATIAL COHERENCE, 2x2 CELLS
Day 2, Region: (150,300)
AVHRR Channel 4
Standard Deviation
0
1
2
3
4
5
6
7
8
250
260
270
280
290
Mean
Dynamic threshold
middle-level cloud
open water/sea ice
Cloud fraction = 0.25

Fig. 3

APPENDIX I

Arctic Cloud Cover Simulated by the Goddard Institute for Space Studies General Circulation Model

Robert G. Crane

Report
Submitted to Dr. Roger G. Barry
Cooperative Institute for Research in Environmental Sciences

December 1987

1. Introduction

Most General Circulation Model (GCM) sensitivity experiments show a marked high latitude response to external forcing such as changes in the solar constant, changes in atmospheric CO_2, or experiments with glacial boundary conditions. The implication of all of these experiments is that the polar regions may play a significant role in global climate and may also be one of the first places to demonstrate present or future climate change.

Climatic processes in the Arctic are dominated by the presence of sea ice--primarily through the effect on the surface albedo and ocean-atmosphere heat exchange--and by the polar cloud cover. Unfortunately, neither sea ice nor cloud cover are particularly well treated in many GCM's, and in the case of the cloud cover the observational data are also very limited.

The role of cloud cover in climate has been discussed by Crane and Barry (1984) with a particular focus on the polar regions. The Arctic cloud cover is known to have a large seasonal variability increasing from about 40-60% in winter to 80-90% in summer (Huschke, 1969). This large increase in summer is attributed, in part, to a shift in the cyclone tracks with an increase in the number of low pressure systems that enter the Arctic Basin at this time. It is also assumed that the rapid increase in spring/summer cloud cover is partly due to decreasing ice concentration and increased moisture availability. At present, however, we do not have sufficient observational data to fully support these assumptions. The problems of the satellite retrieval of cloud parameters is being examined in related studies as part of this project; it is the purpose of the present report to

concentrate on the Arctic cloud cover simulations in the Goddard Institute for Space Studies' (GISS) GCM.

2. The GISS GCM

The present study examines the Arctic cloud cover simulated by a control run of the GISS Model II. This model, described in detail in Hansen et al. (1983), has a horizontal resolution of 8 degrees latitude by 10 degrees longitude and 9 atmospheric layers (2 in the boundary layer, 5 in the remainder of the troposphere and 2 in the stratosphere). Snow depth, cloud cover and cloud height are computed in addition to the usual atmospheric variables, and the model includes diurnal and seasonal cycles. The ocean temperatures and the sea ice cover, however, are specified climatologically.

A comparison of the observed and modelled synoptic climatology of the Arctic Basin has been made by Crane and Barry (1988) using this model. The observed pressure fields over the Arctic are compared with those obtained from the model using a classification typing procedure developed by Kirchhofer (1973) and a rotated principal components analysis for both data sets. The analysis shows that the GISS model appears to give a quite realistic simulation of both the spatial and temporal characteristics of the sea level pressure field. Using the same synoptic climatology Barry et al. (1987) suggest that synoptic controls may be an important factor determining the observed cloud amount during the spring and early summer of 1979 and 1980. Cloud cover is derived from the model data in such a way that it is unlikely that a similar synoptic scale study would be valid in this case (see below). Some idea of the relative importance of synoptic

scale advection versus local effects can be obtained, however, by an examination of the monthly data at various levels in the model.

3. The GISS CGM Cloud Scheme

The GISS model calculates both large scale and convective cloud cover. The actual cloud amounts are not saved on the 5-hourly output available from the control run, but they can be inferred from the optical depth which is saved for levels 1 to 7.

Convective Cloud

The convective cloud is obtained as a proportion of the mass of saturated moist air rising from one layer to the next. The scheme computes a cloud fraction which, at each time step, is compared to a random number between 0 and 1. If the random number is less than the cloud fraction, a cloud amount of 1 is assigned for that time step; if the random number is greater than the cloud fraction a cloud amount of zero is assigned. The GISS model, therefore, uses a cloud amount of zero or one at each time step and simulates the effects of fractional cover within a grid box by using full cloud cover for a fractional amount of time. This gives similar results to computing separate radiation calculations using fractional cloud for both the clear and cloudy portions of the grid box, but saves computer time (Hansen et al., 1983).

Large-Scale Clouds

The large-scale cloud is given by the saturated fraction of the grid box, assuming uniform absolute humidity and subgrid scale temperature variation. As with the cumulus cloud, the fractional amount of cloud cover is also compared to a random number and either zero or complete cloud

cover assigned for the time step. No distinction is made between convective and large-scale cloud in the present analysis but, in general, large-scale clouds account for about 80% of the global cloud cover generated by the model (Hansen et al., 1983).

Cloud Optical Depth

In place of the fractional cloud cover, the 5-hourly data give the optical depth at each layer of a grid box in the presence of clouds. That is, a cell has an optical depth of zero if no clouds are present and a value greater than zero in the presence of clouds. The actual optical depth is a function of cloud type, temperature and depth in the atmosphere. For large-scale cloud, if the layer temperature is less than 258 K the optical depth is given as .33 to match the observational data of Platt (1975) which indicates that cirrus clouds typically have an optical depth of 0.25 - 0.5. Otherwise the optical depth is proportional to the pressure thickness of the layer containing the cloud. For convective cloud the optical depth is .08 times the pressure thickness giving an optical depth of about 8 per 100 mb of thickness. Where both large-scale and convection clouds are present in a cell, the largest optical depth is used.

Determination of Cloud Cover Fraction

While the optical depth of cloud is obviously the important factor in terms of radiative calculations, this is difficult to compare with observations that are made in the form of fractional cloud cover. For the present study, the fractional cloud cover is obtained from the optical depth data by averaging over time.

The cloud optical depths are used to produce a binary map of cloud cover at each level; that is, for optical depth > 0. cloud cover = 1, for

optical depth = 0. cloud cover = 0. The binary grids are used to produce low, middle and total cloud cover; low cloud is cloud in levels 1 or 2 (from the surface to about 850 mb), middle cloud is cloud in levels 3 and 4 (about 850 mb to 550 mb), and total cloud includes cloud at any level. The binary grids of low, middle, and total cloud are averaged over 30 days (150 grids). The time average gives a fractional amount which is similar to the original monthly cloud clover fraction calculated by the model (Figures 1 and 2).

4. Results

The monthly average cloud cover fraction for the Arctic north of 72^{o}N is shown in Figure 3a. This shows a seasonal cycle having a summer maximum similar to that of Huschke (1969) (Figure 4), but with much lower values. At the same time, the winter values are much higher in the model showing that the seasonal range in the model cloud cover for the central Arctic is much less than the observations would suggest. Figure 3b shows the seasonal cycle for the area north of about 55^{o}N and in this case the cycle is reversed with less cloud in the summer months. This reversal in the seasonal cycle is also demonstrated on a regional basis although both the western Arctic (135^{o}W-135^{o}E) and the Canadian Arctic (45^{o}W-135^{o}W) show very little seasonal variability (Figure 5), and most of the variation occurs in the European sector (45^{o}W-45^{o}E) and the Kara/Laptev Sea (45^{o}E-135^{o}E). In these regions the seasonal cycle is again reversed with less cloud in the summer months. These regions extend from approximately 86^{o}N to 55^{o}N and should not, therefore, be compared with the regional data of Huschke. The change in the seasonal cycle reflects the change in cyclone tracks as they move further north in summer; the decrease in the

regional cloud fractions being matched by an increase in the central Arctic fraction (Figures 3a and 5d). This seasonal variability is further illustrated in the cloud maps for January and July (Figures 6 and 7). In January the largest cloud fractions are found in the higher mid-latitudes primarily in the North Pacific region and in the NE Atlantic, while in July the greater cloud cover occurs north of about 70°N. The July distribution of total cloud cover for the Arctic agrees with Gorshkov (1980) in that there is a relative maximum at high latitudes with the largest fractions being in the north Atlantic region. However, there is a major difference in the Central Arctic where Gorshkov shows 90% cloud cover while the model has a relative minimum with less than 60% cloud cover. One should note, however, that the model values for June and August are much higher (Figure 5e) and that we are only examining one year of model output.

Comparing Figures 6a-c it is apparent that the regions of largest low, middle and total cloud cover coincide suggesting that cloud cover is controlled by the large scale processes. We should also note, however, that the low cloud fraction is much higher than either Voskresenskiy and Chukanin (1959) or Vowinckel and Orvig (1970) find for the Eastern Arctic. Figures 7a-c for July, on the other hand, show the higher levels of low, total and middle cloud coinciding in the western Arctic and North Atlantic, but with an area of increased low cloud north and west of the Taymyr Peninsula where ice concentrations have already begun to decrease in the model.

The minimum ice extent in the model occurs in September with low ice concentrations (less than 30%) in the southern Barents/Kara Sea and along the Beaufort Coast. Ice concentrations of less than 50% are found along

the Siberian coast and ice concentrations between 75% and 85% are found in the Beaufort up to about 78°N and the Barents Sea up to about 86°N. The September cloud cover shows a general decrease over the July figures with the largest cloud cover fractions being found further south once more. For the most part there is a general agreement between the low, middle and total cloud, but again there are areas which have a relative maximum in low cloud and a minimum in middle cloud corresponding to the regions of low ice concentration in the Barents/Kara Sea and, to some extent, along the Beaufort Coast. There are extensive areas of low cloud in the Canadian Arctic and the East Siberian Sea, but these also coincide with regions of extensive middle cloud as well.

Although it cannot be demonstrated conclusively, these results do suggest that the decreased ice concentration in the Seasonal Sea Ice Zones of the Eastern Arctic and along the Beaufort Coast do contribute to increased low level cloudiness in the model. For the most part, however, the Arctic cloud cover does appear to be controlled by the larger scale processes.

5. Summary and Conclusions

The GISS model cloudiness in the polar region of the Northern Hemisphere demonstrates the seasonal variability that would be expected from the observational data, but at a much reduced range for the Central Arctic. As with the observational data, the zone of maximum cloud cover moves north in the summer, but actual amounts are less than expected by about 10-20%.

Barry et al. (1987) suggest that there is a strong synoptic control on

cloud cover amounts in the Arctic which is supported by the more detailed microphysical studies of Jayaweera (1982) who also suggests that the lower stratus layers may be formed by the lifting of fog over sea ice, while the upper layers are a response to large-scale southerly flow. In the case of the GISS model, while most of the cloud cover would appear to be due to large-scale processes, there is some evidence that reduced ice concentration in summer does give rise to some increased low level cloud on a limited regional basis. One final consideration is that during the early summer, when the model is already showing too little cloud in the Arctic, there is also a tendency for mid-latitude aerosols to be transported to the Arctic resulting in the presence of optically thick Arctic Haze (Rahn, 1985). This again may have some further effect on the surface and lower tropospheric energy balance in the Arctic.

Acknowledgment

This work was supported under NASA Climate Research Grant NAG 5-898 to Roger G. Barry. We are indebted to Dr. J. Hansen for providing the GISS Model data.

References

Barry, R. G., Crane, R. G., Schweiger, A. and Newell, J., 1987. Arctic Cloudiness in Spring From Satellite Imagery. **J. Climatology**, 7: 423-451.

Crane, R. G. and Barry, R. G., 1984. The Influence of Clouds on Climate with a Focus on High Latitude Interactions. **J. Climatology**, 4: 71-93.

Crane, R. G. and Barry, R. G.; 1988. Comparison of the MSL Synoptic Pressure Patterns of the Arctic as Observed and Simulated by the GISS General Circulation Model. Submitted to **Met. and Atmos. Phys.**

Gorshkov, S. G. (ed) 1980. **World Ocean Atlas. Vol 3, Arctic Ocean.** Dept. of Navigation and Oceanography, Ministry of Defence, USSR (Pergamon Press, Oxford, 1983).

Hansen, J., Russell, G., Rind, D., Stone, P., Lacis, A., Lebedeff, S., Ruedy, R. and Travis, L., 1983. Efficient Three-Dimensional Global Models for Climate Studies: Models I and II. **Mon. Wea. Rev.**, 111: 609-662.

Kirchhofer, W., 1973. Classification of 500 mb Patterns. **Arbeit der Schweizer Meteorolo. Zentral.**, 45: 16 pp.

Platt, C. M. R., 1975. Infrared Emissivity of Cirrus-Simultaneous Satellite, Lidar and Radiometric Observations. **Quart. J. Roy. Met. Soc.**, 101: 119-126.

Rahn, K. A. (ed) 1985. Arctic Air Chemistry. **Atmos. Environ.**, 19.

Vowinckel, E. and Orvig, S., 1970. The Climate of the North Polar Basin. In Orvig, S. (ed) **World Survey of Climatology**, 14, 129.

Voskresenskiy, A. I. and Chukanin, K. I., 1959. Meteorologicheskie Usloviya Obled Eneiya v Oblakov Tipa st is sc. **Trudy Arkticheskogo i Antarkticheskogo Nauchno-Issledovatel'skogo Instituta**, 228: 124.

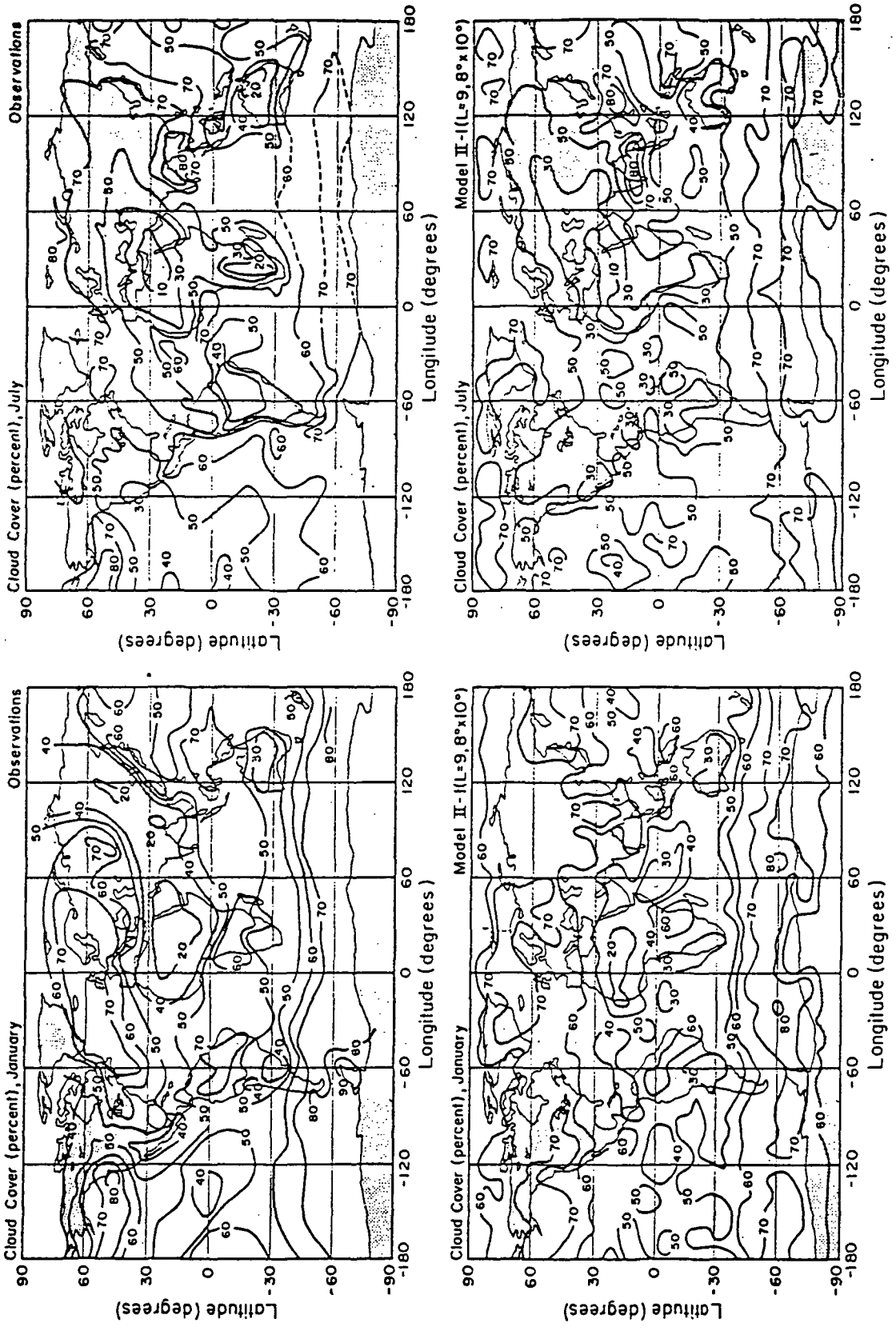

Figure 1. Modelled and Observed Cloud from Hansen et al. (1983)

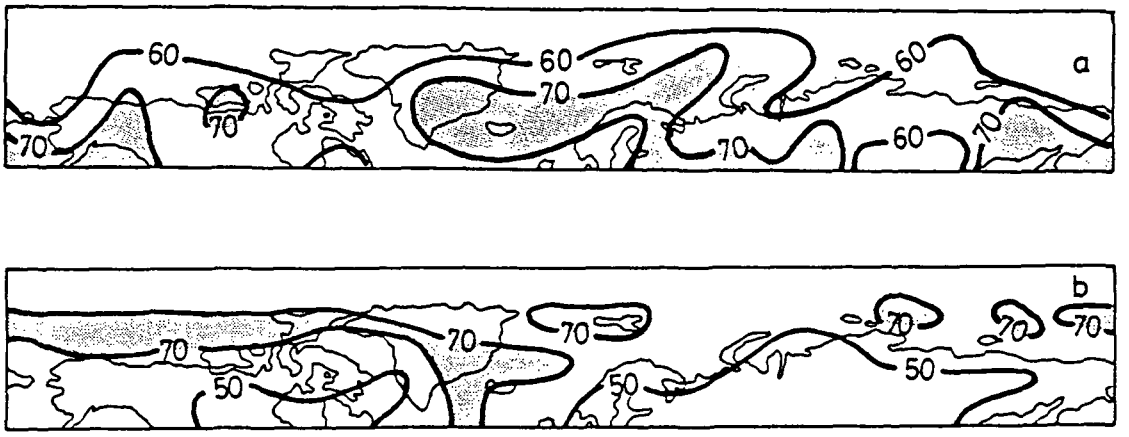

Figure 2. January (a) and July (b) Total Cloud Cover From the Present Study (shaded areas have greater than 70% cloud cover)

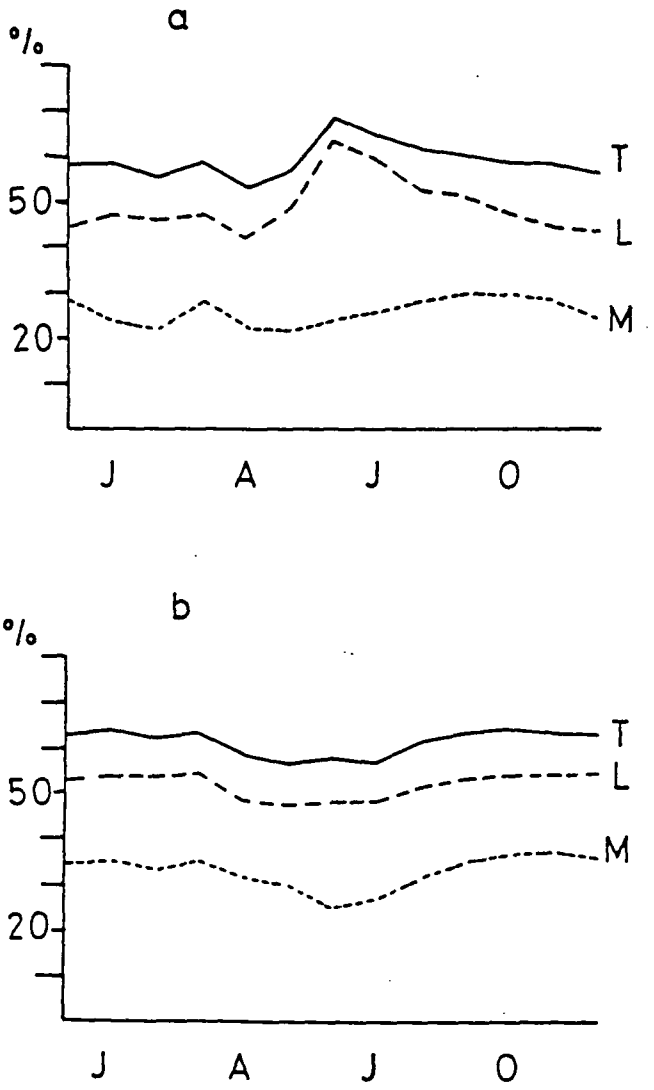

Figure 3. Seasonal Cycle of Cloud Cover for the Arctic North of 72N (a) and North of 65N (b)

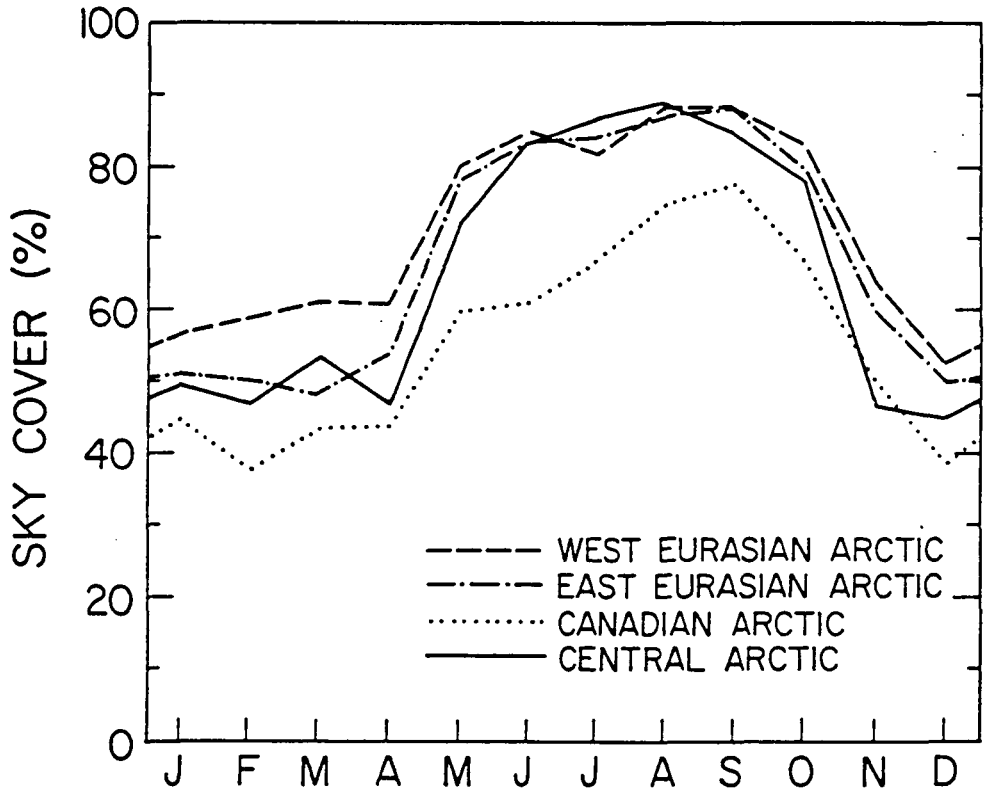

Figure 4. Monthly Cloud Cover For the Arctic (Huschke, 1969)

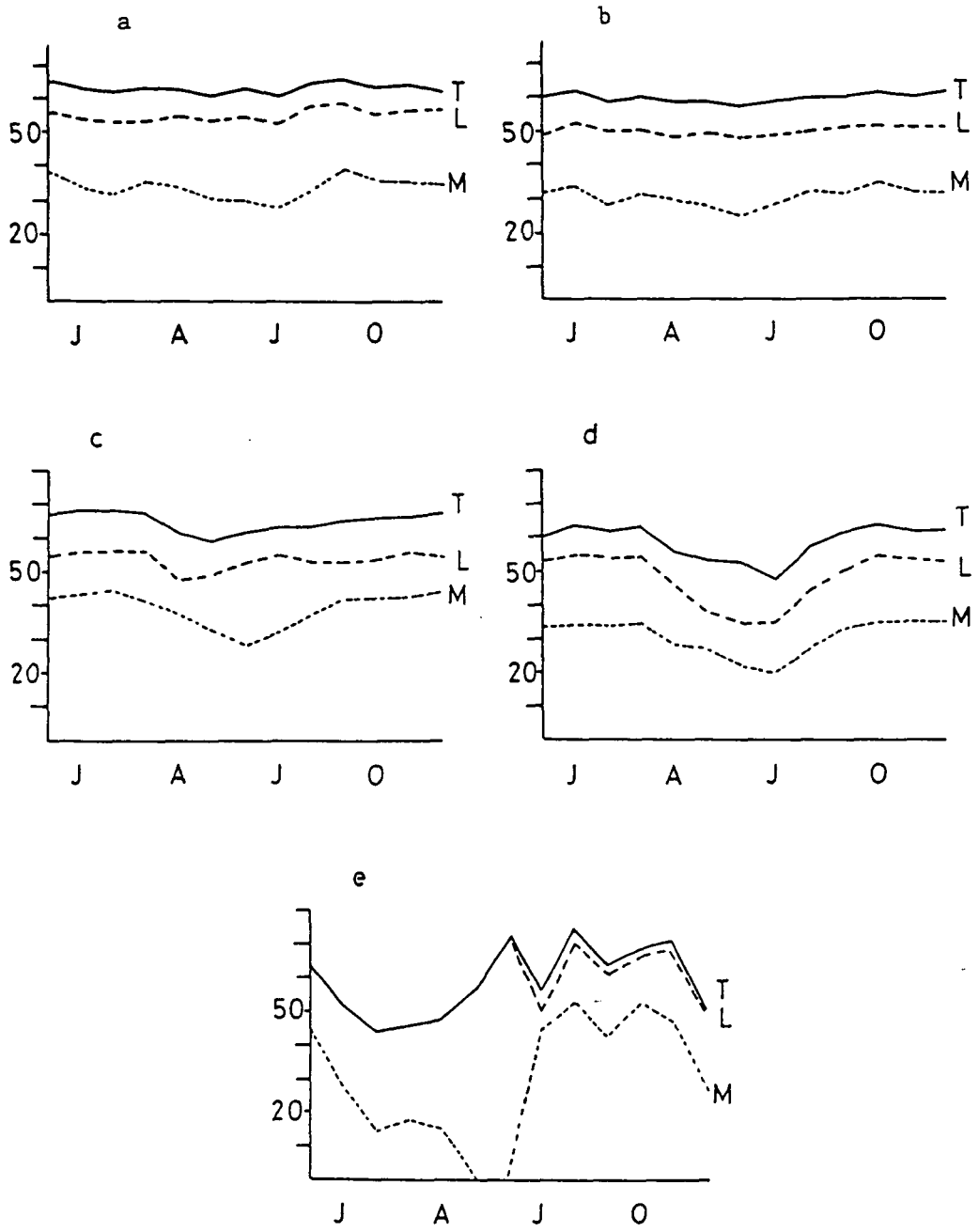

Figure 5. Monthly Cloud Cover (GISS Model) For a) the Western Arctic, b) Canadian Arctic, c) European Arctic, d) Laptev Sea, and e) the North Pole

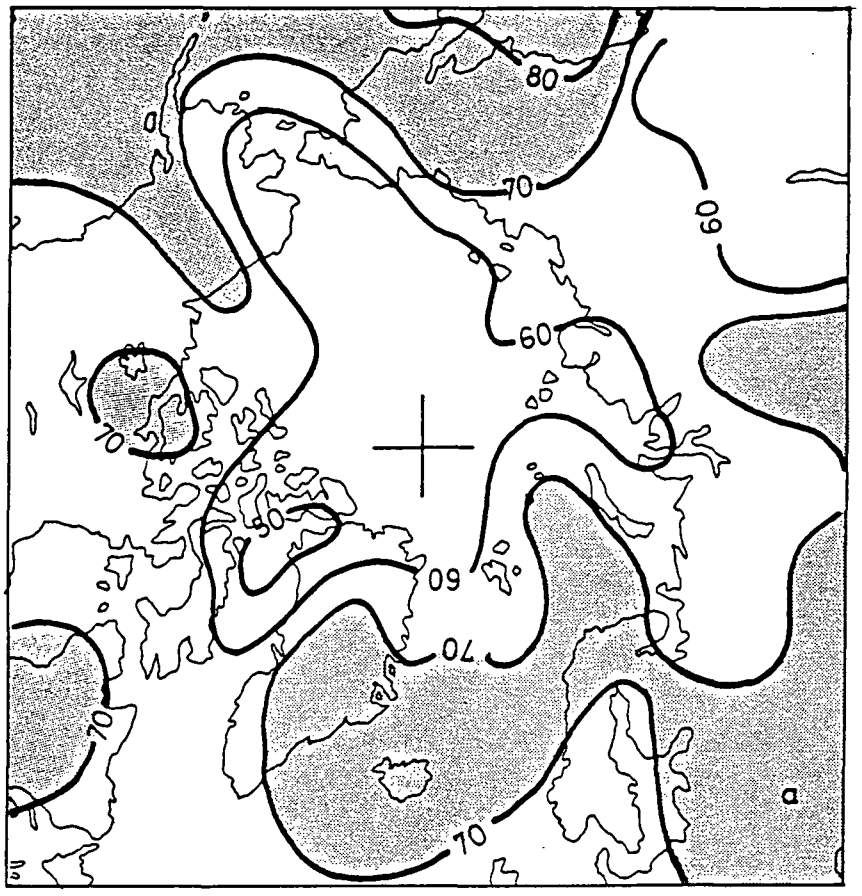

Figure 6. Mean January Cloud Cover From the GISS GCM.
(a) Total Cloud (shaded areas = greater than 70% cloud)
(b) Low Cloud (shaded areas = greater than 60% cloud)
(c) Middle Cloud (shaded areas = greater than 40% cloud)

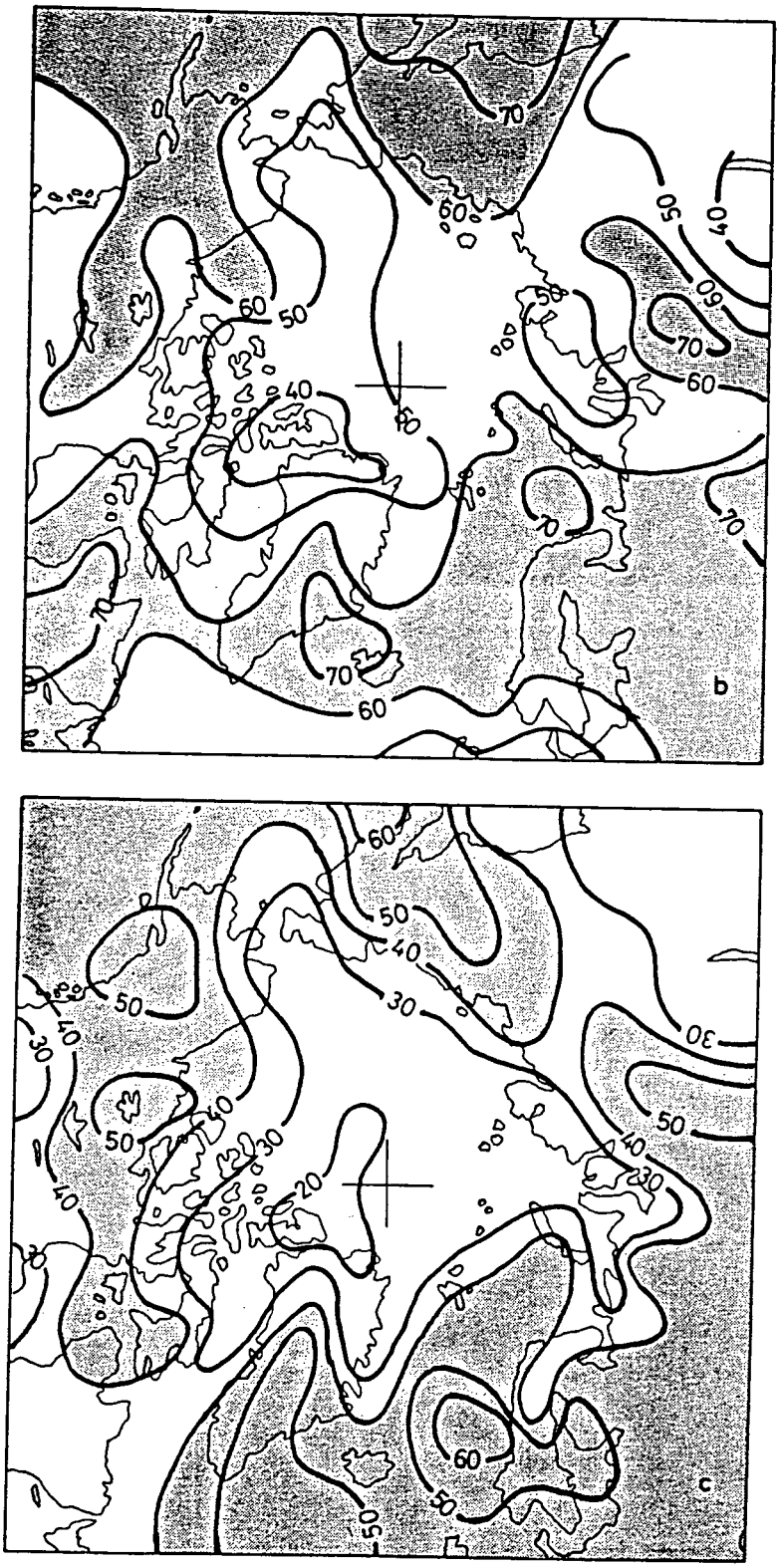

Figure 6. Continued

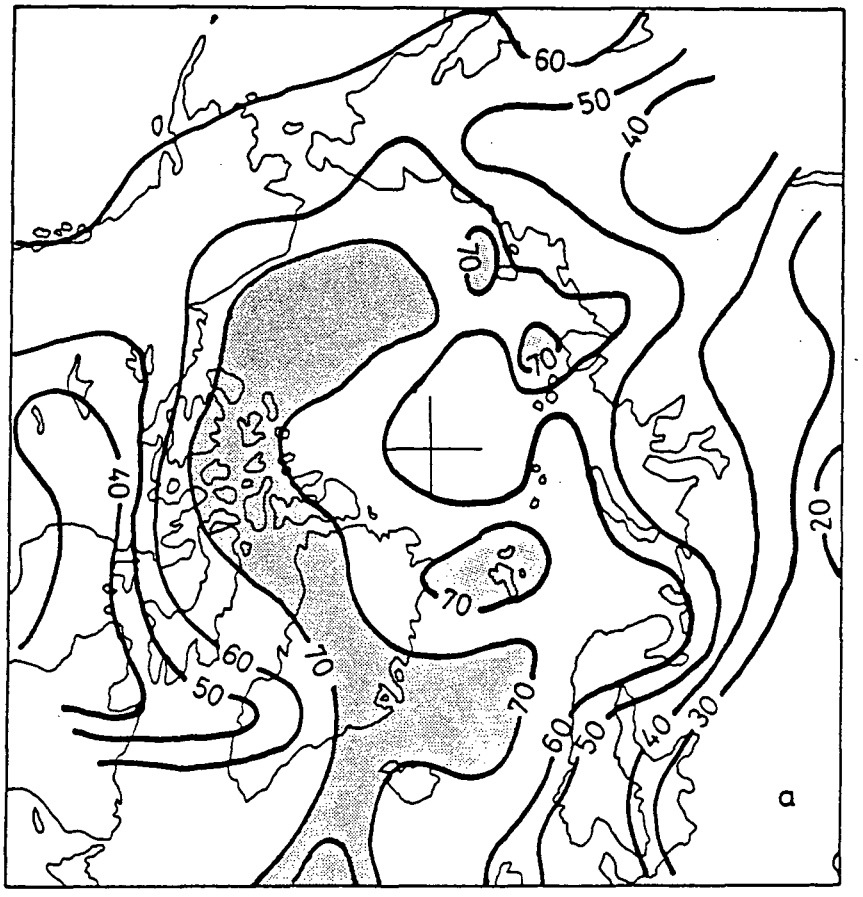

Figure 7. Mean July Cloud Cover From the GISS GCM.
(a) Total Cloud (shaded areas = greater than 70% cloud)
(b) Low Cloud (shaded areas = greater than 60% cloud)
(c) Middle Cloud (shaded areas = greater than 40% cloud)

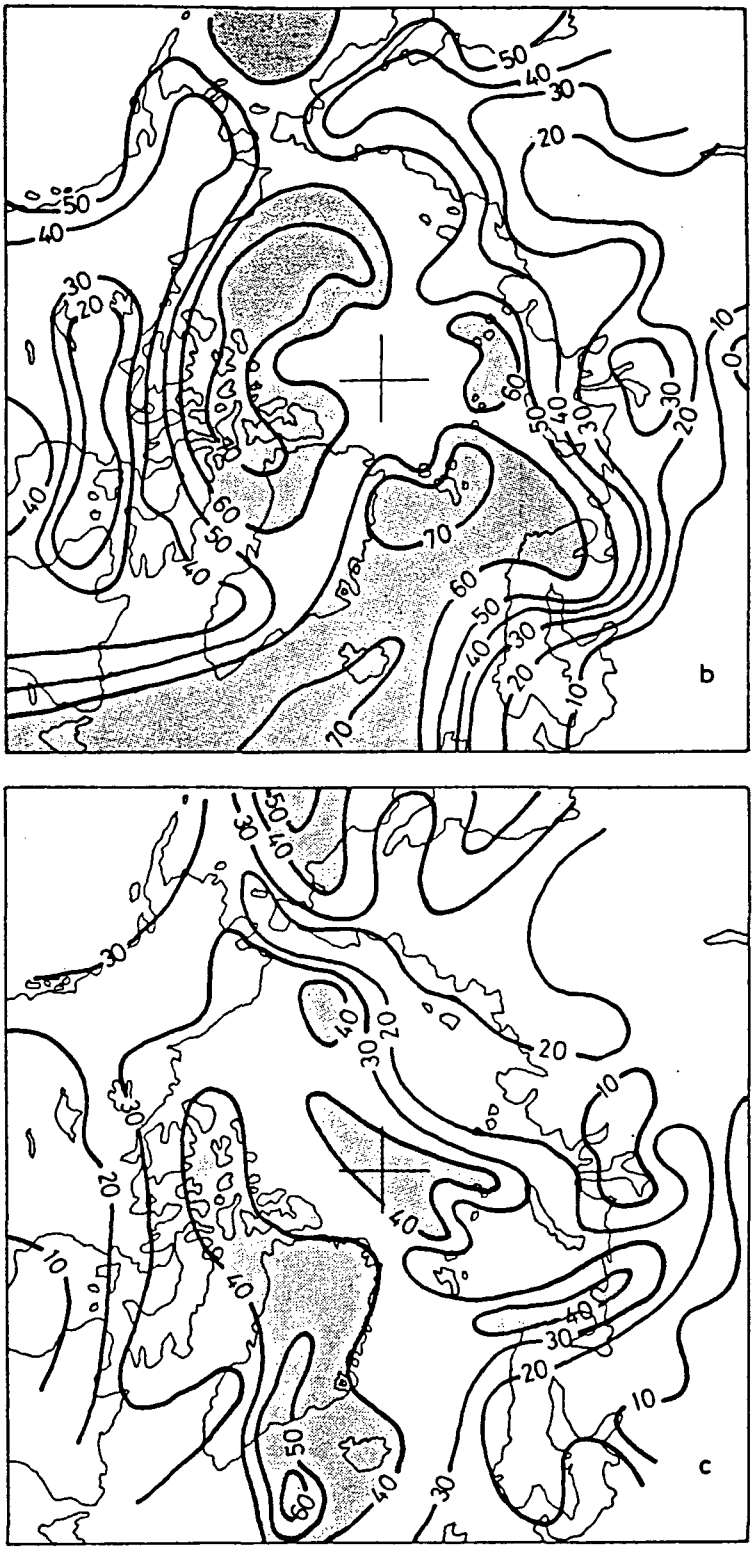

Figure 7.. Continued

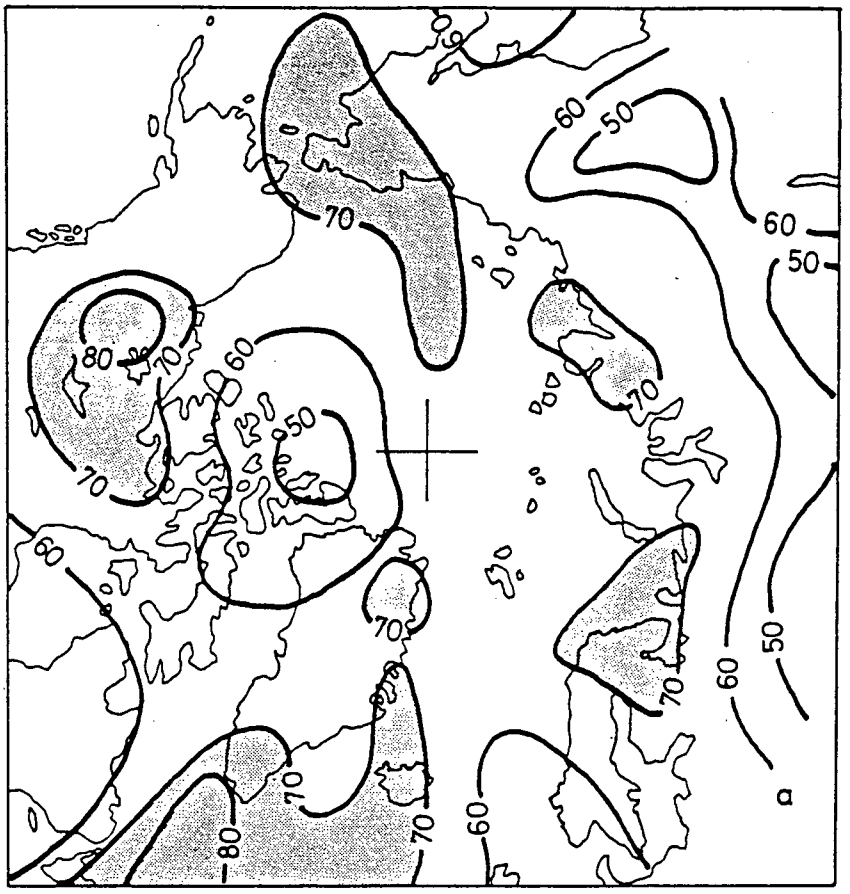

Figure 8. Mean September Cloud Cover From the GISS GCM.
(a) Total Cloud (shaded areas = greater than 70% cloud)
(b) Low Cloud (shaded areas = greater than 60% cloud)
(c) Middle Cloud (shaded areas = greater than 40% cloud)

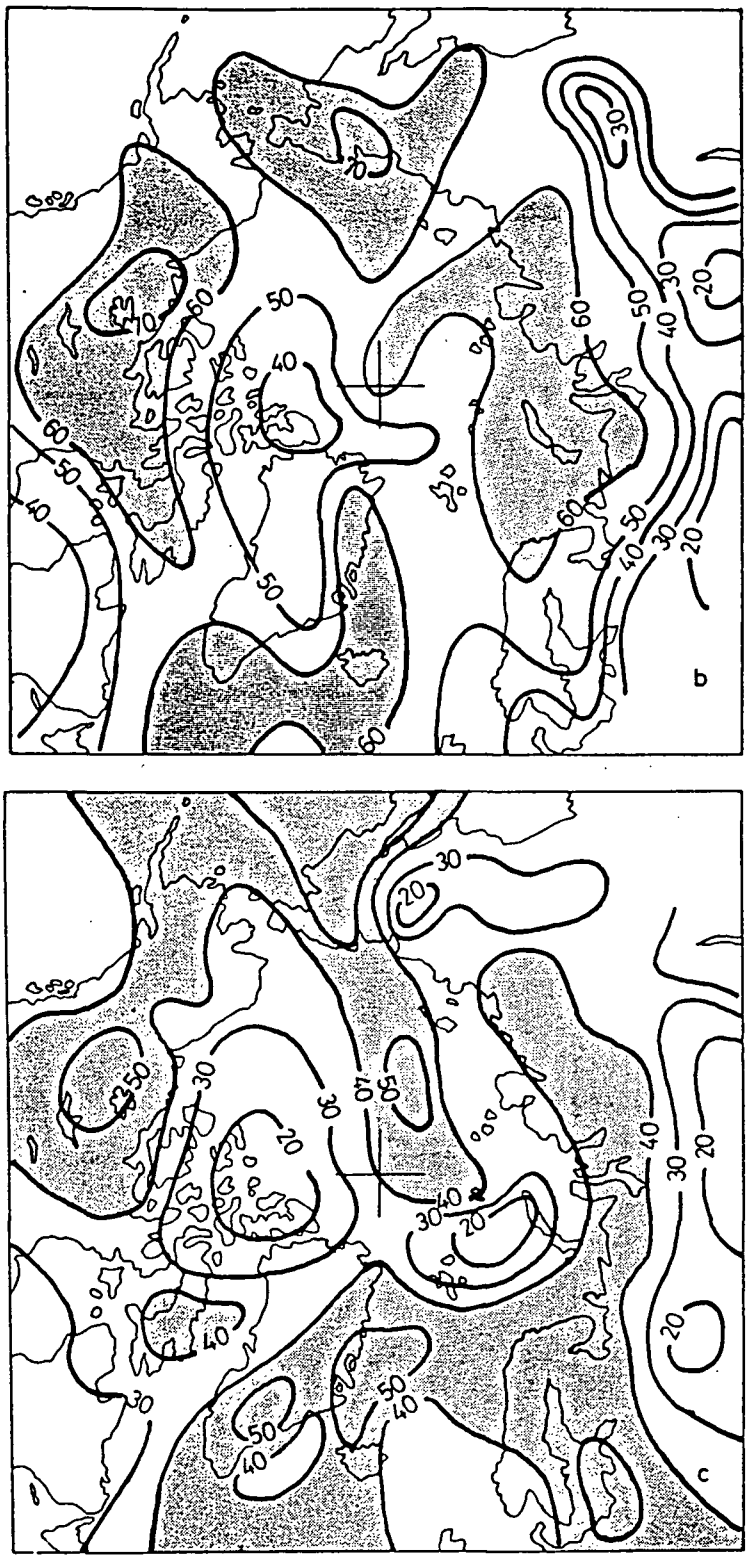

Figure 8. Continued

APPENDIX II
Submitted to Int. Journal of Remote Sensing Letters

MERGING AVHRR AND SMMR DATA FOR REMOTE SENSING OF ICE AND CLOUD IN POLAR REGIONS

J.A. Maslanik, J.R. Key, and R.G. Barry
Cooperative Institute for Research in Environmental Sciences
and Department of Geography
University of Colorado, Boulder
Campus Box 449
Boulder, Colorado 80309-0449

ABSTRACT

Multispectral data from AVHRR are digitally processed and merged with multi-frequency, dual-polarized passive microwave imagery acquired by the Nimbus-7 SMMR. Five channels of AVHRR data, four channels of SMMR brightness temperatures, and SMMR-derived ice concentration and ice type are navigated and co-registered to a polar stereographic grid. The merged data sets are currently being used in combination with meteorological information for integrated studies of clouds and sea ice.

1. Introduction

The important role that polar processes play in the dynamics of global climate is widely recognized (Earth Systems Science Committee 1986). Remote-sensing of the distribution and characteristics of clouds and sea ice is required to detect and monitor variability in the Arctic and Antarctic, as well as to provide input to climate models.

Optical-wavelength sensors provide high spatial resolution, but are limited by the long periods of darkness, poor lighting conditions, and persistent cloud cover common in polar regions. Passive microwave sensors operate independently of solar illumination, can view the surface through cloud cover, and provide surface information not contained in visible or thermal imagery. However, existing passive microwave sensors yield relatively poor spatial resolution. A combination of digital multispectral data appears to be a logical way of capitalizing on the unique capabilities of each sensor, while overcoming some of the problems inherent in remote sensing at high latitudes. This work outlines the creation of a set of merged digital data consisting of optical, infrared, and thermal imagery from NOAA's Advanced Very High Resolution Radiometer (AVHRR) and passive microwave imagery from the Nimbus-7 Scanning Multichannel Microwave Radiometer (SMMR) into a form suitable for the analysis of cloud and sea ice cover.

2. AVHRR Data

The AVHRR sensors carried onboard the TIROS-N and NOAA series of satellites sample the earth in 4 or 5 spectral channels, with a nadir resolution of 1.1 km (IFOV of 1.4 milliradians) at a satellite altitude of 833 km (NOAA 1984). The channels are 1: 0.58-0.68 m (relected visible), 2: 0.725-1.00 m (reflected visible and near IR), 3: 3.55-3.93 m (reflected/emitted thermal IR), 4: 10.3-11.30 m (emitted thermal IR), 5: 11.5-12.50 m (emitted thermal IR). The data used in this study are derived from the standard Polar Orbiter Level 1b archive (NOAA 1984), and consist of partial orbits of Global Area Coverage (GAC) imagery. This is a reduced-resolution product created through on-board satellite proc
essing to yield a nadir resolution of slightly better than 4 km. GAC data files contain calibration parameters, pixel location in latitude and longitude, and solar zenith angle information. Data values are recorded in 10 bits.

AVHRR 5-channel GAC imagery for January 6-13 and July 1-7, 1984 covering areas with snow, ice, ocean, and land, and including a variety of cloud types over different surfaces are used in this study. First-order calibration of the AVHRR GAC data was performed using the calibration coefficients contained in the image files and the methods described in the NOAA Polar Orbiter Users Guide (NOAA 1984) and in Lauritsen, et al. (1979). Coefficients for the thermal channels (channels 3, 4, and 5) are generated in-flight using a stable blackbody as a warm source,

and space as the cold source. The data values recorded in channels 1-5 were converted to approximate spectral albedo in percent for channels 1 and 2, and radiance in milliwatts/m^2-steradians-cm^{-1} for channels 3-5. These conversions were performed as a linear function, with slope and intercepts provided by the calibration coefficients contained in the data. The thermal radiances were also converted to physical temperature in Kelvins, or brightness temperature, using an approximation of the inverse of the Planck function. The percent reflectance values produced for channels 1 and 2 by this method are approximations of albedo. Care is required when comparing these values to broad-band albedos sensed over a wider spectral range (Hughes and Henderson-Sellers 1982).

No adjustment for atmospheric effects were made with the exception of the solar zenith angle corrections described below. The typically low water vapor content in polar atmospheres, as well as the low physical temperature of the atmosphere, reduces most atmospheric effects to a point where they may be neglected for the type of analysis performed here.

To account at least in part for the significant effects of solar zenith angle differences along the wide swath of AVHRR, the digital number for each channel 1 and channel 2 pixel was normalized by dividing the pixel value by the cosine of the solar zenith angle for that pixel as provided in the GAC data records. Since only one zenith angle is provided per 8 data pixels, the intermediate zenith angles were interpolated linearly to yield an

approximate angle for each pixel.

A final step in the AVHRR data correction involved extracting the reflected-energy component from the emitted component in channel 3. At 3.7 micrometers, this channel records both reflected and emitted energy. Brightness temperatures estimated from channel 4 were converted to channel 3 expected radiances using an inverse calculation of the Planck approximation with channel 3 parameters. Subtraction of these radiances from the actual radiances measured in channel 3 yields the component of energy in channel 3 attributable to reflection.

3. Passive Microwave Data

Passive microwave data used in this study were acquired on January 6, 8, and 10 and July 2, 4 and 6, 1984 by the Scanning Multichannel Microwave Radiometer (SMMR) on Nimbus 7 (Gloersen and Barath, 1977). The SMMR collects data in five microwave channels (6.6 GHz, 10.7 GHz, 18.0 GHz, 21.0 GHz, and 37.0 GHz), with two polarizations (horizontal and vertical) per channel. Instantaneous field of view of the sensor varies with channel, ranging from 148 x 95 km for the 6.6 GHz channel to 55 x 41 km and 27 x 18 km for the 18 and 37 GHz channels, respectively.

The SMMR data used in this study consist of data that had been converted from orbital format to a polar stereographic projection. The dual-polarized 18 and 37 GHz data are mapped to grid cells with a dimension of 25 x 25 km true at 70° latitude. The 18 GHz are interpolated to accommodate the 25 km resolution

grid. During the gridding process, no distinction is made between day, night, and twilight orbits, and data from overlapping orbits are averaged to yield a daily value. The data stored in these grids are recorded as brightness temperature in Kelvins.

4. Combining AVHRR and SMMR Data

Merging of the AVHRR GAC imagery and the SMMR passive microwave data required selection of a common grid size that offered a compromise between resolution and data volume. A polar stereographic projection yielding equal-area pixels true at 70° latitude was selected as the desired map base, with a 5 km grid cell (pixel) size. This pixel size represents a slight degradation of the AVHRR GAC resolution, but has the advantage, in terms of data processing, of being an even multiple of the SMMR 25 x 25 km cells. The SMMR data were converted to 5 km cell sizes by simple duplication of pixels, thereby avoiding any artificial "improvement" in resolution. Sea ice concentration and old ice fraction were calculated from the SMMR data using the NASA Team Algorithm (Cavalieri, et al. 1984). This algorithm is based on the normalized difference between vertically- and horizontally-polarized emissivity at 18 GHz.

Re-mapping of the AVHRR data to the polar projection was performed using the ground locations in latitude and longitude provided in the GAC records. Latitude and longitude coordinates for the intermediate pixels were interpolated linearly from each

eighth-pixel location and transformed from latitude/longitude to polar grid coordinates using standard map projection algorithms. Unfilled grid cells were interpolated by an average of non-zero neighbors. At the edges of the orbit swath, the reduction in true ground resolution due to the earth's curvature is reflected by pixel duplication that yields larger "effective" pixels, although the grid cell size remains constant across the rectified polar-stereographic image. Since one of the ultimate objectives of this project is to investigate viewing angle dependencies on observed reflectivity and temperature, no adjustments were made to compensate for these viewing angle effects. Accuracy of the AVHRR navigation using this method is expected to be within 25 km, or roughly the equivalent of an individual SMMR pixel.

In order to maintain as much radiometric resolution in the data as possible, the AVHRR and SMMR imagery were typically stored and processed in 16-bit form.

5. Applications

An example of a calibrated and registered AVHRR channel 1 image centered approximately on Novaya Zemlya, and covers the Kara and Barents Seas is given in Figure 1. Figure 2 illustrates the SMMR data (37 GHz horizontal) for the same area. Resolution differences and differences in information content between the two sensors are obvious. The color-composite of AVHRR channels 1 and 4, and SMMR-derived ice concentration shown in Figure 3 demonstrates the ability to map ice concentration and ice edge

position beneath cloud cover.

The merged AVHRR-SMMR data sets are proving useful for a variety of applications that benefit from near-simultaneous observations of clouds and surfaces. Currently, these data are being used to determine the spectral and textural properties of clouds over different concentrations and conditions of sea ice. Other applications include analysis of directional reflectance and emittance differences, the investigation of the relationship between SMMR-derived ice concentration and AVHRR-measured albedo, comparison of ice concentration and ice-edge position as estimated by AVHRR and SMMR, and comparison of AVHRR-derived physical temperatures with physical temperature and emissivity estimated from SMMR.

These studies will aid in the adaptation of the cloud analysis algorithm of the International Satellite Cloud Climatology Project (ISCCP) for use in polar regions (Rossow et al., 1985). In particular, the SMMR and SMMR-derived data sets are useful in the determination of surface type, a crucial step in the algorithm. Although still in the testing and development stage, this application of the combined data sets has already shown that the surface often changes within the five- and thirty-day time periods over which the ISCCP algorithm operates, violating one of its basic assumptions. Future work will investigate the utility of passive microwave data merged with the Level B3 AVHRR product to be archived as part of ISCCP (Schiffer and Rossow, 1985).

6. Conclusion

The ability to retrieve information on albedo, physical temperature, and brightness temperature from spatially and temporally co-located imagery is proving to be a useful aid in comparing the spectral and textural properties of ice and clouds in a broad range of the energy spectrum. The merged data sets offer a means of capitalizing on the unique capabilities of AVHRR and passive microwave data by reducing the inherent limitations of each sensor (e.g., illumination requirements, cloud cover, and low resolution).

ACKNOWLEDGMENTS

This work was supported under NASA grant NAG-5-898 and DOD University Research Instrumentation Program grant N00014-85-C-0039. Thanks are due to W. Rossow and E. Raschke for providing AVHRR GAC data.

References

Brown, O.B., Brown, J.W., and Evans, R.H. 1985, Calibration of Advanced Very High Resolution Radiometer infrared observations. J. Geophys. Res., 90, No. C6, 11667-11677.

Cavalieri, D.J., Gloersen, P., and Campbell, W.J. 1984, Determination of sea ice parameters with Nimbus-7 SMMR. J. Geophys. Res., 88, 5355-5369.

Earth System Science Committee 1986, Earth system science: a program for global change. NASA Advisory Council Report, Earth System Science Committee.

Gloersen, P. and Barath, F.T. 1977, A scanning multichannel microwave radiometer for Nimbus-G and Seasat-A. IEEE J. of Oceanic Engr., OE-2 (2), 172-178.

Hughes, N.A. and Henderson-Sellers, A. 1982, System albedo as sensed by satellites: its definition and variability. Int. J. Remote Sensing, 3 (1), 1-11.

Lauritson, L., Nelson, G.J., and Porto, F.W. 1979, Data extraction and calibration of TIROS-N/NOAA radiometers, NOAA Tech. Memo, TM NESS 107, 81 pp.

NOAA 1984, NOAA polar orbiter data users guide. U.S. Dept. of Commerce, National Oceanic and Atmospheric Administration, NESDIS, February, 1984.

Rossow, W.B., Mosher, F., Kinsella, E., Arking, A., Desbois, M., Harrison, E., Minnis, P., Ruprecht, E., Seze, G., Simmer, C., and Smith, E. 1985, ISCCP cloud algorithm intercomparison, J. Clim. Appl. Meteor., 24, 877-903.

Schiffer, R.A. and Rossow, W.B., 1985, ISCCP global radiance data set: A new resource for climate research, Bull. Am. Met. Soc., 66(12), 1498-1505.

Figures

Figure 1: Calibrated and registered AVHRR channel 1 image centered approximately on Novaya Zemlya, and covering the Kara and Barents Seas.

Figure 2: SMMR 37 GHz horizontal data for the same area shown in Figure 1.

Figure 3: A composite of AVHRR channels 1 and 4, and SMMR-derived ice concentration for the areas shown in Figure 1.

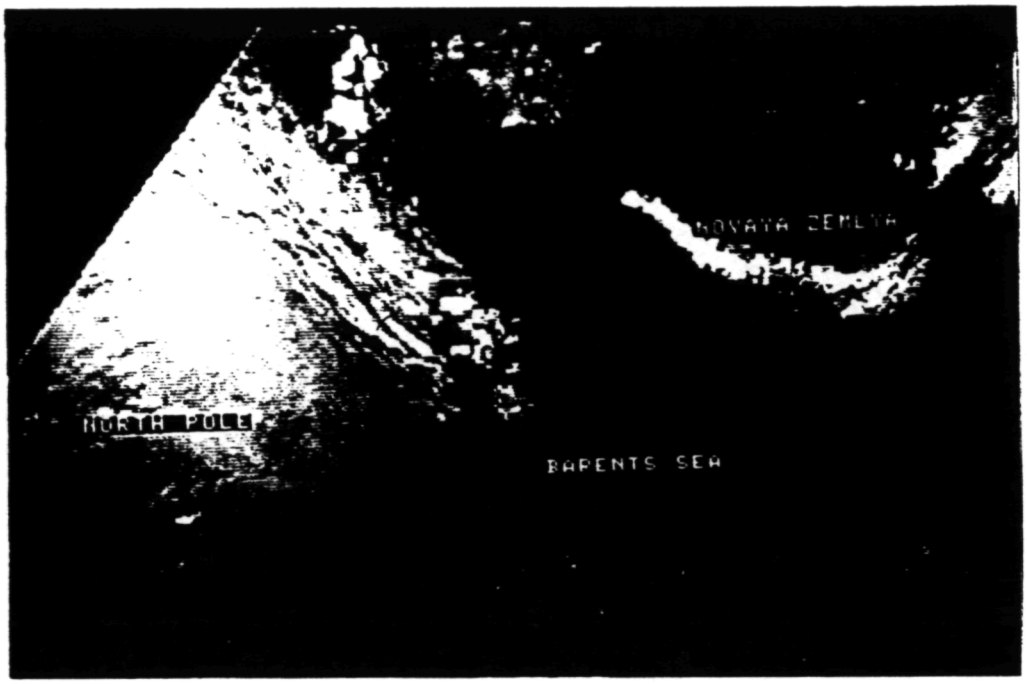

Publications Supported in Whole or Part by NAG-5-898

Barry, R.G., Crane, R.G., Newell, J., and Schweiger, A., 1988. "Arctic cloudiness in spring from satellite imagery. A response," **J. Climatol.**, in press.

Crane, R.G. and Barry, R.G., 1988. "Comparison of the MSL synoptic pressure patterns of the Arctic as observed and simulated by the GISS General Circulation Model," **Meteor. Atmos. Physics**, in press.

Maslanik, J.A., Barry, R.G., and Crane, R.G., 1987. "Approaches to the interpretationof cloud cover in the polar regions," (abstract). Clouds in Climate II. (A WCRP Workshop on Modeling and Observations, Columbia, MD). WCRP, NASA, NSF, NOAA, and DOE, p. 169.

McGuffie, K., Barry, R.G., Newell, J., Schweiger, A., and Robinson, D., 1988. "Intercomparison of satellite-derived cloud analyses for the Arctic Ocean in spring and summer," **Int. J. Remote Sensing**, 9 (3), 467-477.